JACS
JOURNAL OF THE AMERICAN CHEMICAL SOCIETY
Article
Cite This: J. Am. Chem. Soc. 2018, 140, 8526−8534
pubs.acs.org/JACS

Charge Delocalization and Bulk Electronic Conductivity in the Mixed-Valence Metal−Organic Framework Fe(1,2,3-triazolate)$_2$(BF$_4$)$_x$

Jesse G. Park,[†] Michael L. Aubrey,[†] Julia Oktawiec,[†] Khetpakorn Chakarawet,[†] Lucy E. Darago,[†] Fernande Grandjean,[⊥] Gary J. Long,[⊥] and Jeffrey R. Long*[,†,‡,§]

[†]Department of Chemistry, University of California, Berkeley, California 94720, United States
[⊥]Department of Chemistry, Missouri University of Science and Technology, University of Missouri, Rolla, Missouri 65409-0010, United States
[‡]Department of Chemical and Biomolecular Engineering, University of California, Berkeley, California 94720, United States
[§]Materials Sciences Division, Lawrence Berkeley National Laboratory, Berkeley, California 94720, United States

Supporting Information

ABSTRACT: Metal−organic frameworks are of interest for use in a variety of electrochemical and electronic applications, although a detailed understanding of their charge transport behavior, which is of critical importance for enhancing electronic conductivities, remains limited. Herein, we report isolation of the mixed-valence framework materials, Fe(tri)$_2$(BF$_4$)$_x$ (tri$^-$ = 1,2,3-triazolate; x = 0.09, 0.22, and 0.33), obtained from the stoichiometric chemical oxidation of the poorly conductive iron(II) framework Fe(tri)$_2$, and find that the conductivity increases dramatically with iron oxidation level. Notably, the most oxidized variant, Fe(tri)$_2$(BF$_4$)$_{0.33}$, displays a room-temperature conductivity of 0.3(1) S/cm, which represents an increase of 8 orders of magnitude from that of the parent material and is one of the highest conductivity values reported among three-dimensional metal−organic frameworks. Detailed characterization of Fe(tri)$_2$ and the Fe(tri)$_2$(BF$_4$)$_x$ materials via powder X-ray diffraction, Mössbauer spectroscopy, and IR and UV−vis-NIR diffuse reflectance spectroscopies reveals that the high conductivity arises from intervalence charge transfer between mixed-valence low-spin Fe$^{II/III}$ centers. Further, Mössbauer spectroscopy indicates the presence of a valence-delocalized Fe$^{II/III}$ species in Fe(tri)$_2$(BF$_4$)$_x$ at 290 K, one of the first such observations for a metal−organic framework. The electronic structure of valence-pure Fe(tri)$_2$ and the charge transport mechanism and electronic structure of mixed-valence Fe(tri)$_2$(BF$_4$)$_x$ frameworks are discussed in detail.

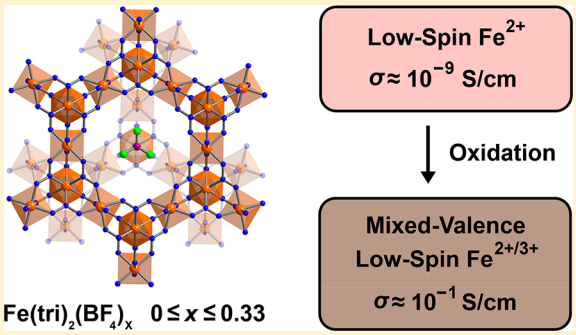

INTRODUCTION

Metal−organic frameworks are modular, three-dimensional network solids constructed from metal ions and rigid, polytopic organic linkers.[1] This modularity can endow metal−organic frameworks with impressive porosities, surface chemistry, and chemical stability,[2] and, consequently, these frameworks are being extensively investigated for applications ranging from gas separations and storage to drug delivery.[3] Within the past decade, engendering bulk electronic conductivity in metal−organic frameworks has also become of interest as a means of extending their potential application as battery electrode materials, electrochemical sensors, and electrocatalysts.[4]

However, many of the features that render metal−organic frameworks advantageous as porous storage and separation materials also present a challenge to their application in electronic devices that require high conductivity. Indeed, the characteristically low crystal densities of metal−organic frameworks imply large distances between atoms along most lattice vectors. Such materials inherently favor electronic structures with particularly weak band dispersion because valence orbital overlap (an ad hoc indicator of bulk dispersion) diminishes exponentially with interatomic distance.[5] Thus, charge carriers in metal−organic frameworks can generally be expected to have extremely large effective masses yielding local electronic structures of a near-molecular nature.[6] Indeed, to date there have been only a few literature examples of metal−organic frameworks that exhibit both permanent porosity and a high electronic conductivity.[7]

Among many notable efforts to increase charge transport in these materials, one attractive strategy is the development of frameworks consisting of either repeating mixed-valence, redox-active metal centers or redox-active linkers.[8,9] The use of mixed-valency can at a minimum locally improve charge mobility on neighboring atoms; in most mixed-valence frameworks, the electronic substructures are indeed localized and may reasonably be described as small polarons, akin to an

Received: April 5, 2018
Published: June 12, 2018

DOI: 10.1021/jacs.8b03696
J. Am. Chem. Soc. 2018, 140, 8526−8534

isolated Marcus-type coupling interaction.[10] Nonetheless, with a contiguous path along at least one dimension of the framework lattice, the resulting hopping-type charge mobility can still engender a relatively high conductivity.[10a,11] For instance, a ferric semiquinoid−quinoid framework was recently shown to exhibit a three-dimensional conductivity of 0.16 S/cm, arising from a combination of ligand-based mixed-valence supported by 3*d*-π orbital interactions through bridging iron(III) centers.[9g] Likewise, a number of other frameworks have been found to be conductive owing to charge delocalization across mixed-valence ligand centers.[9]

Metal-centered mixed-valence has been extensively investigated in many solid state systems, such as iron oxides, iron sulfides, iron cyanides, Prussian Blue compounds, manganese perovskites, and titanates, to name a few.[12] In addition, mixed-valence first-row transition metal coordination solids have been shown to exhibit electronic delocalization.[13] Engendering high electronic conductivity in three-dimensional metal−organic frameworks by taking advantage of metal-centered valence delocalization may thus hold promise. However, early examples of such frameworks have typically displayed conductivity values much lower than frameworks with ligand-centered charge carriers, and thus there is likely much room for improvement.[7g,8]

In pursuit of promising systems with the potential for exhibiting metal-centered mixed-valence, we identified the framework $Fe(tri)_2$ (tri^- = 1,2,3-triazolate), a previously reported material with an intriguing electronic structure arising from octahedrally coordinated Fe^{II} centers bridged by π-acidic azolate ligands (Figure 1).[8c] Previously, $Fe(tri)_2$ was reported to exhibit an intrinsic conductivity of 7.7×10^{-5} S/cm, which further increased to 1.0×10^{-3} S/cm following vapor diffusion of I_2 through the material. This reported conductivity for the as-synthesized $Fe(tri)_2$ is surprisingly high, given the closed-shell nature of low-spin iron(II) and the triazolate linker, as noted elsewhere.[7g,14] As such, $Fe(tri)_2$ was determined to be an excellent candidate for exploring the relationship between metal-centered mixed-valence and conductivity in a porous solid.

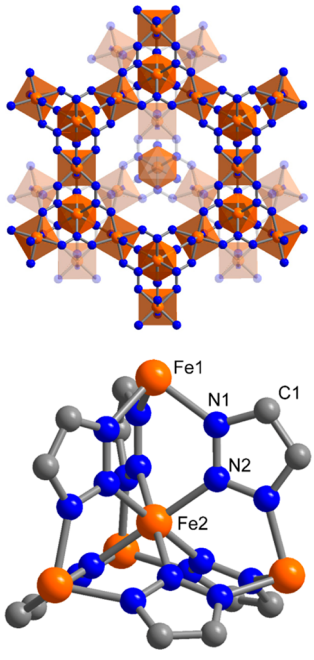

Figure 1. Fe−N sublattice (top) and a tetrahedral secondary building unit of $Fe(tri)_2$ (bottom). Orange, blue, and gray spheres represent Fe, N, and C atoms, respectively; H atoms have been omitted for clarity.

Herein, we present the rigorous air-free synthesis of $Fe(tri)_2$, together with its mixed-valence derivatives, $Fe(tri)_2(BF_4)_x$ (x = 0.09, 0.22, and 0.33), obtained through postsynthetic stoichiometric oxidation reactions. Physical characterization then enables insight into the charge transport behavior underlying the impressive enhancement in the conductivity of these materials with increasing oxidation level.

EXPERIMENTAL SECTION

General Considerations. Unless otherwise noted, all manipulations were carried out in an argon atmosphere in an Mbraun MB200MOD glovebox. Glassware was oven-dried at 150 °C for at least 4 h and allowed to cool in an evacuated glovebox antechamber prior to use. Dimethylformamide (DMF), acetonitrile (MeCN), and dichloromethane were dried using a commercial solvent purification system made by JC Meyer Solvent Systems and stored over 3- or 4-Å molecular sieves prior to use. Anhydrous $FeCl_2$ beads (99.9% purity) were purchased from Sigma-Aldrich. The 1,2,3-triazole ligand (98% purity) was purchased from VWR International LLC, deoxygenated with three freeze−pump−thaw cycles, and stored over 4-Å molecular sieves prior to use. The synthesis of $Fe(tri)_2$ was carried out using a modification of the previously reported procedure.[8c] Instead of performing the reaction in an evacuated sealed tube, it was carried out in an Ar-filled glovebox using 20 mL vials. Thianthrenium tetrafluoroborate was synthesized as previously described.[15] Carbon, hydrogen, and nitrogen elemental analyses were obtained from the Microanalytical Laboratory at the University of California, Berkeley. Inductively coupled plasma atomic emission spectrometry (ICP-AES) analysis for iron and boron were obtained from Galbraith Laboratories, Inc.

Synthesis of Fe(1,2,3-triazolate)$_2$(BF$_4$)$_{0.33}$. A purple solution of thianthrenium tetrafluoroborate (0.158 g, 0.520 mmol) in 10 mL of MeCN was added to neat pink crystalline powder $Fe(tri)_2$ (0.200 g, 1.04 mmol), and the mixture was stirred at 25 °C for 16 h. The resulting suspension was filtered to yield a light brown powder. The powder was washed by soaking in two successive 15 mL aliquots of MeCN for 24 h, and was then dried under reduced pressure (13 μbar) at 120 °C for 48 h to yield 0.222 g (97% yield) of product as a brown microcrystalline solid. Anal. Calcd for $FeC_4H_4N_6B_{0.33}F_{1.32}$: C, 21.78; H, 1.83; N, 38.09. Found: C, 21.78; H, 1.78; N, 37.6. ICP-AES Found: Fe:B, 1:0.33.

Synthesis of Fe(1,2,3-triazolate)$_2$(BF$_4$)$_x$ (x = 0.025, 0.05, 0.09, 0.22). Similar procedures were followed as above. See Supporting Information (SI) for details.

RESULTS AND DISCUSSION

Synthesis and Characterization of Fe(tri)$_2$. The synthesis of $Fe(tri)_2$ was carried out in 20 mL vials in a glovebox under an Ar atmosphere, in a modification of the previously reported procedure.[8c] Special caution was taken during the synthesis and handling of $Fe(tri)_2$, as even slight air-exposure or the use of a partially oxidized $FeCl_2$ source led to the isolation of an orange or light brown colored powder, instead of the pale pink powder characteristic of the valence-pure phase. Successful synthesis of phase-pure $Fe(tri)_2$ was confirmed by powder X-ray diffraction analysis,[8c,16] and Le Bail refinement of the diffraction data enabled identification of the space group as $Fd\bar{3}m$ and resulted in a lattice parameter of a = 16.6423(6) Å.

The structure of activated $Fe(tri)_2$ was obtained by Rietveld refinement of the synchrotron powder X-ray diffraction pattern

DOI: 10.1021/jacs.8b03696
J. Am. Chem. Soc. 2018, 140, 8526−8534

(see Figure S6) and is composed of octahedral Fe^{II} centers bridged by μ_3-1,2,3-triazolate ligands (Figure 1). Here, two crystallographically distinct Fe^{II} centers form tetrahedral pentanuclear repeat units that share vertices to form a diamondoid structure type. A single, adamantane-like cage of the structure is depicted in Figure 1. The Fe1−N1 and Fe2−N2 distances, where Fe1 and Fe2 correspond to the tetrahedral corner and center iron(II) sites, respectively, are 1.961(2) and 1.977(3) Å, consistent with Fe−N distances for compounds with low-spin Fe^{II} ions and strong-field ligands.[17] Metal−organic frameworks exhibiting low-spin Fe^{II} centers are quite rare in the literature, although there have been several reports suggesting that triazolate-based ligands can stabilize low-spin octahedral Fe^{II} centers in zero-,[18] one-,[19] and three-dimensional[20] coordination compounds.

Slow-Scan Cyclic Voltammetry of $Fe(tri)_2$. Slow-scan cyclic voltammetry experiments were carried out to investigate the redox behavior of $Fe(tri)_2$. This technique has been commonly used to characterize redox-active intercalation solids.[21] By observing the current response arising from scanning potentials with sufficiently slow rates, it is possible to probe the process of bulk ion insertion into a solid. In addition, a precise stoichiometry of the entire active material can be determined by current integration.

By using the equipment described in the SI, a slow-scan cyclic voltammogram (CV) of $Fe(tri)_2$ was obtained (Figure 2). Oxidation and reduction processes occur between 2.9 and

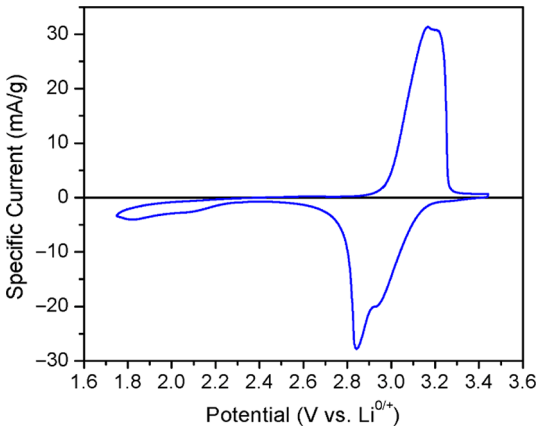

Figure 2. Slow-scan cyclic voltammogram of $Fe(tri)_2$ collected at a scan rate of 50 μV/s in an electrolyte solution of 1 M $LiBF_4$ in propylene carbonate. Lithium was used as a reference and counter electrode.

3.3 and 2.6−3.2 V vs $Li^{0/+}$ with corresponding charge capacities of 30.8 and 28.2 mAh/g, respectively. The oxidative feature most likely corresponds to oxidation of the Fe^{II} centers to Fe^{III} and the voltage composition profile obtained for $Fe(tri)_2$ between 2.6 and 3.4 V suggests that $Fe(tri)_2(BF_4)_x$ can be oxidized quasi-reversibly from $x = 0$ to $x = 0.22$ with an efficiency of 92% (Figure S2). The predicted stoichiometry is lower than expected for complete oxidation of the Fe^{II} centers that would correspond to $x = 1$, potentially owing to the small pore size of $Fe(tri)_2$, which may limit BF_4^- ion insertion.

Chemical Oxidation of $Fe(tri)_2$. Motivated by the quasi-reversible $Fe^{II/III}$ redox features observed in the slow scan CV of $Fe(tri)_2$, we performed stoichiometric chemical oxidations of the framework using thianthrenium tetrafluoroborate in MeCN (Scheme 1). Reaction of $Fe(tri)_2$ with 0.1, 0.25, and 0.5

Scheme 1. Post-Synthetic Chemical Oxidation of $Fe(tri)_2$ with Thianthrenium Tetrafluoroborate

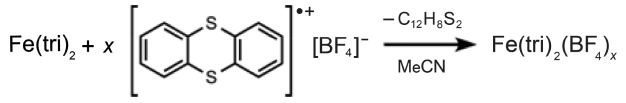

equiv of the oxidant resulted in isolation of light brown, brown, and dark brown microcrystalline powders, respectively. For the products isolated using 0.1 and 0.25 equiv of oxidant, ICP-AES analysis revealed Fe:B ratios of 1:0.09 and 1:0.22, respectively, indicating near-stoichiometric conversions. However, when 0.5 equiv of oxidant were added, the solution was observed to retain the purple color of unreacted thianthrenium tetrafluoroborate even after the reaction had proceeded for 16 h, suggesting that oxidation of $Fe(tri)_2$ did not go to completion. Indeed, analysis of the product isolated from this reaction via ICP-AES revealed a Fe:B ratio of only 1:0.33, consistent with a substoichiometric oxidation. We note that $x = 0.33$ is the stoichiometry expected if each andamantly-like pore within the framework structure is filled with a single BF_4^- ion.

Brunauer-Emmet-Teller (BET) surface areas of 230, 70, and 50 m^2/g were calculated for the activated $Fe(tri)_2(BF_4)_x$ materials with $x = 0.09$, 0.22, 0.33, respectively, using N_2 adsorption data collected at 77 K (Figure S3). Here, the diminishing surface areas are consistent with the increasing presence of charge-balancing BF_4^- anions in the pores relative to the parent $Fe(tri)_2$ framework, which exhibits a BET surface area of 370 m^2/g. The very low surface area determined from a type II isotherm of $Fe(tri)_2(BF_4)_{0.33}$ suggests that the compound is essentially nonporous, consistent with the lack of any calculated accessible surface area (see Table S1), and therefore that N_2 adsorption occurs solely on the outer surfaces of the crystallites. Both ICP-AES and N_2 adsorption isotherm data indicate that the pore size of $Fe(tri)_2$ precludes counteranion insertion beyond 0.33 equiv and therefore further oxidation.

Characterization of the activated $Fe(tri)_2(BF_4)_x$ ($x = 0.09$, 0.22, 0.33) materials using powder X-ray diffraction revealed that the parent framework structure is maintained upon oxidation, with no evidence of decomposition (Figure 3). Le Bail refinement of the diffraction patterns yielded lattice parameters of $a = 16.6136(7)$, 16.5140(5), and 16.4368(5) Å for $x = 0.09$, 0.22, and 0.33, respectively, indicating a

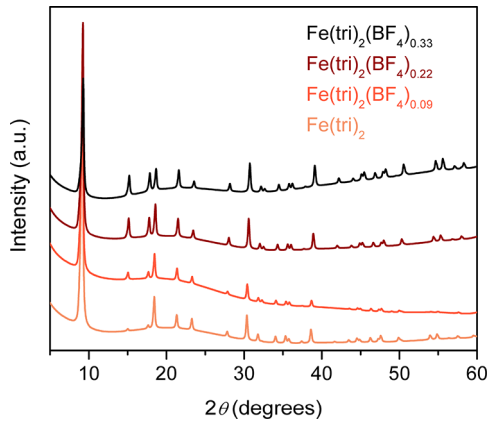

Figure 3. Powder X-ray diffraction patterns for $Fe(tri)_2$ and $Fe(tri)_2(BF_4)_x$ obtained with a wavelength of 1.5418 Å.

DOI: 10.1021/jacs.8b03696
J. Am. Chem. Soc. 2018, 140, 8526−8534

contraction of the unit cell upon chemical oxidation (Table S2). A plot of lattice constants vs x follows a nearly linear trend that is qualitatively consistent with Vegard's law (Figure S5), implying that each $Fe(tri)_2(BF_4)_x$ material behaves as a single phase with a homogeneous distribution of BF_4^- ions.

The crystal structures of activated $Fe(tri)_2(BF_4)_{0.33}$ at 300 and 100 K determined by Rietveld refinement using synchrotron powder X-ray diffraction patterns (see Figures S7 and S8) are shown in Figures S9 and S10, respectively, and reflect a slight contraction of the unit cell with decreasing temperature (see Table S3 for the fit parameters). However, the significant structural distortion that would be anticipated to accompany charge localization is not apparent. Comparing the structures of $Fe(tri)_2$ and $Fe(tri)_2(BF_4)_{0.33}$ obtained at 300 K, a small decrease occurs in the Fe1−N1 distance from 1.961(2) to 1.938(3) Å, as expected for a partial oxidation of low-spin iron(II) to low-spin iron(III).[17] In contrast, the Fe2−N2 distance changes only negligibly (i.e., within uncertainty) from 1.977(3) to 1.971(3) Å, suggesting that oxidation occurs primarily at the corner Fe1 sites. Given that the two unique iron sites experience similar ligand fields based upon the Mössbauer spectrum of $Fe(tri)_2$ (vide infra), the apparent preferential oxidation at the Fe1 site may result from the geometrical constraints imposed at the iron ions, with low-spin iron(III) favoring the corner Fe1 site due to a greater freedom there to distort away from an ideal octahedral coordination geometry. A slight contraction of the unit cell and the corresponding supertetrahedra occurs upon framework oxidation, as is evidenced by a decrease in the Fe1···Fe1 separation from 5.8869(4) to 5.8263(8) Å. Difference Fourier maps generated from the $Fe(tri)_2(BF_4)_{0.33}$ diffraction data also indicated the presence of charge-balancing BF_4^- ions, with a single ion present in the pores of the framework. These BF_4^- ions refine to full occupancy, again suggesting that oxidative insertion of further BF_4^- ions is not possible in $Fe(tri)_2$.

Mössbauer Spectroscopy. The ^{57}Fe Mössbauer spectra of $Fe(tri)_2$ and $Fe(tri)_2(BF_4)_x$ obtained at 290 K are shown in Figure 4 (see Table S4 for the corresponding fitting parameters). At 290 K, $Fe(tri)_2$ exhibits a single component spectrum that was best fit with a narrow symmetric quadrupole doublet with a line width, Γ, of 0.267(5) mm/s, an isomer shift, δ, of 0.385(1) mm/s, and a small quadrupole splitting, ΔE_Q, of 0.084(7) mm/s. Each of these parameters are consistent with the presence of low-spin iron(II)[12c] in a highly symmetric pseudo-octahedral nitrogen coordination environment. Although the measured line width is similar to the calibration line width of the spectrometer, the two inequivalent crystallographic iron(II) sites in $Fe(tri)_2$ are not resolved in the spectrum. This absence suggests that the two iron(II) sites in $Fe(tri)_2$ experience very similar ligand fields.

The 290 K Mössbauer spectra of $Fe(tri)_2(BF_4)_x$ also exhibit very similar narrow quadrupole doublet components that are assigned to the Fe2 low-spin iron(II) site (Figure 4, red lines; the corresponding hyperfine parameters are given in Table S4). However, an additional absorption at approximately −0.1 mm/s clearly begins to grow in as x increases. This absorption was fit as part of a symmetric doublet (Figure 4, blue lines) and the corresponding hyperfine parameters are given in Table S4. For all values of x, the isomer shift of this component is smaller than that of the red component, which suggests that the blue component can be assigned to the Fe1 intermediate valence iron(II/III) ion. The percent areas of the blue quadrupole doublets were found to be 16.2(5), 50.8(6), and 66.67% for x = 0.09, 0.22, and 0.33, respectively, in reasonable agreement with twice the expected iron(III) stoichiometry (based upon the empirical formula for each material). Hence, at 290 K the blue doublets are assigned to valence averaged low-spin iron(II/III) sites, between which the delocalized electron is averaged on the Mössbauer time scale of $\sim 10^{-8}$ s[22] (corresponding to the period of the precession of the iron-57 nuclear quadrupole moment within its electron electric field

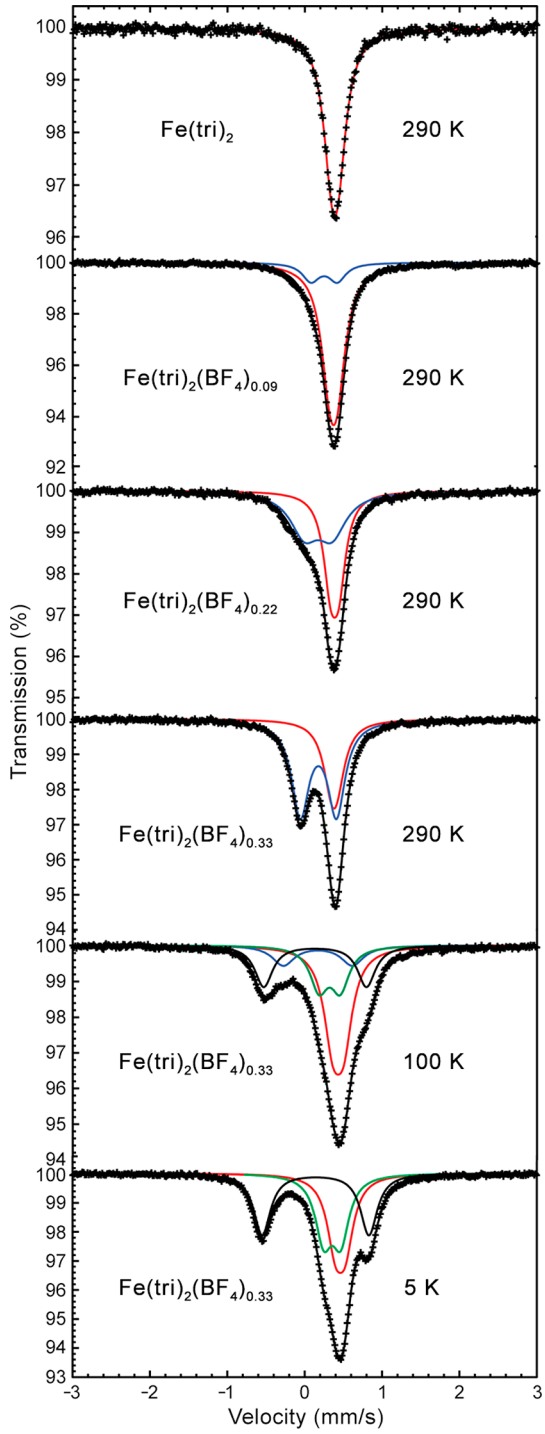

Figure 4. Mössbauer spectra of $Fe(tri)_2$ and $Fe(tri)_2(BF_4)_x$ obtained at the indicated temperatures. The component doublets correspond to low-spin iron(II) (red trace), valence-delocalized low-spin iron(II/III) (blue trace), localized low-spin iron(II) (green trace), and localized low-spin iron(III) (black trace).

DOI: 10.1021/jacs.8b03696
J. Am. Chem. Soc. 2018, 140, 8526−8534

gradient). For x = 0.22 and 0.33, Mössbauer spectra collected at various temperatures down to 5 K (vide infra), reveal that this doublet persists down to 150 and 100 K, respectively.

A consideration of the structural data obtained from powder X-ray diffraction studies suggests this valence averaging most likely occurs over the four Fe1 tetranuclear vertices that surround the central Fe2 crystallographic site at a distance of 5.8263(8) Å (see the lower portion of Figure 1). Additionally, from an examination of the triazolate ligand resonance structures, it is clear that electronic coupling between the two N1 sites via π-3d orbital conjugation would be preferable over coupling between N1 and N2, despite the closer corresponding Fe1···Fe2 distance. At room temperature, these valence-averaged Fe1 sites are indistinguishable by crystallography and Mössbauer spectroscopy. Furthermore, since the Fe1 centers occupy shared vertices in the extended structure, they are likely responsible for promoting charge mobility between adjacent supertetrahedra and ultimately throughout the entire crystal. While such delocalization behavior has been observed previously in minerals and molecular compounds containing mixed-valence $Fe^{II/III}$ centers, this is a rare example of such an observation in a metal–organic framework.[12,13]

To further support the above assignments and investigate the electron delocalization, Mössbauer spectra were also obtained for $Fe(tri)_2(BF_4)_{0.22}$ and $Fe(tri)_2(BF_4)_{0.33}$ at various temperatures between 5 and 295 K (see Figure S11 and Figure 4, respectively, and Table S4 for the corresponding fit parameters). At 5 K, no electron delocalization is expected and the Mössbauer spectra of both $Fe(tri)_2(BF_4)_{0.22}$ and $Fe(tri)_2(BF_4)_{0.33}$ were accordingly fit with three doublets: one assigned to the static, low-spin iron(II) site, Fe2 (red trace), and two assigned to the portion of the Fe1 sites that are low-spin iron(II) and low-spin iron(III) at some point on the Mössbauer time scale (green and black traces, respectively). These assignments assume that Fe2 has a static valence and does not participate in the electron delocalization. At 5 K, the sum of the percent areas of the green and black doublets is equal to the percent area of the blue doublet at 290 K, which strongly supports electron localization at 5 K. In contrast, the observation of the blue doublet at 290 K strongly supports electron delocalization at 290 K for x = 0.22 and 0.33.

The Mössbauer spectra of $Fe(tri)_2(BF_4)_{0.22}$ at 150 and 200 K and of $Fe(tri)_2(BF_4)_{0.33}$ at 100 K are more complex, as is revealed in the absorption profile around −0.5 mm/s (Figures S11 and 4, respectively). At these temperatures, the spectra were fit with four quadrupole doublets: the narrow red doublet assigned to the Fe2 low-spin iron(II) site, green and black doublets assigned to valence localized Fe1 low-spin iron(II) and iron(III) sites, and the blue doublet assigned to valence averaged Fe1 low-spin iron(II/III). For x = 0.22, the percent area of the valence average blue doublet increases from 15% at 150 K to 51% at 295 K, indicating increased valence delocalization with increasing temperature. Indeed, the variable-temperature conductivity behavior of $Fe(tri)_2(BF_4)_x$ material (vide infra) may be closely correlated to this temperature dependent valence-localization observed in the Mössbauer spectra of x = 0.22 and 0.33. Additional discussion of the Mössbauer spectra, including the temperature and the x dependence of the spectral parameters, can be found in the SI.

Magnetic Properties of $Fe(tri)_2(BF_4)_{0.33}$. Variable-temperature dc magnetic susceptibility data were collected to investigate the possibility of magnetic ordering in $Fe(tri)_2(BF_4)_{0.33}$. Under an applied magnetic field of 1 T, the 300 K value of the molar magnetic susceptibility (χ_M) times T is 0.406 emu·K/mol, significantly higher than the value of 0.124 emu·K/mol expected for 0.33 equiv of low-spin (S = 1/2) iron(III) per mole of framework (Figure S12). We attribute this difference to substantial contributions from higher-spin excited states, and the field-dependence of the $\chi_M T$ product is consistent with such contributions (Figure S12). With decreasing temperature, $\chi_M T$ decreases gradually from 300 to 20 K and abruptly below 20 K to reach a value of 0.105 emu·K/mol at 3 K. Such behavior is suggestive of antiferromagnetic interactions between low-spin Fe^{III} centers and, indeed, a Curie–Weiss fit to a plot of $1/\chi_M$ versus T in the high-temperature regime (Figure S13) yielded a Curie constant of C = 0.514 emu·K/mol and a Weiss temperature of θ = −80.9 K, consistent with a dominant antiferromagnetic interaction. However, no long-range magnetic ordering was observed down to 3 K (see Figure S14).

UV–vis–NIR Diffuse Reflectance Spectroscopy. UV–vis–NIR diffuse reflectance spectra of $Fe(tri)_2(BF_4)_x$ (x = 0.0, 0.09, 0.22, 0.33) are shown at the top of Figure 5. A weak absorption band in the spectrum for $Fe(tri)_2$ at ν_{max} = 19 900 cm^{-1} is assigned to a low-spin Fe^{II} d–d transition, and with increasing oxidation and the introduction of Fe^{III} centers into the framework this band shifts to higher energies. Note that the $Fe(tri)_2(BF_4)_x$ spectra in Figure 5 were normalized to the d–d

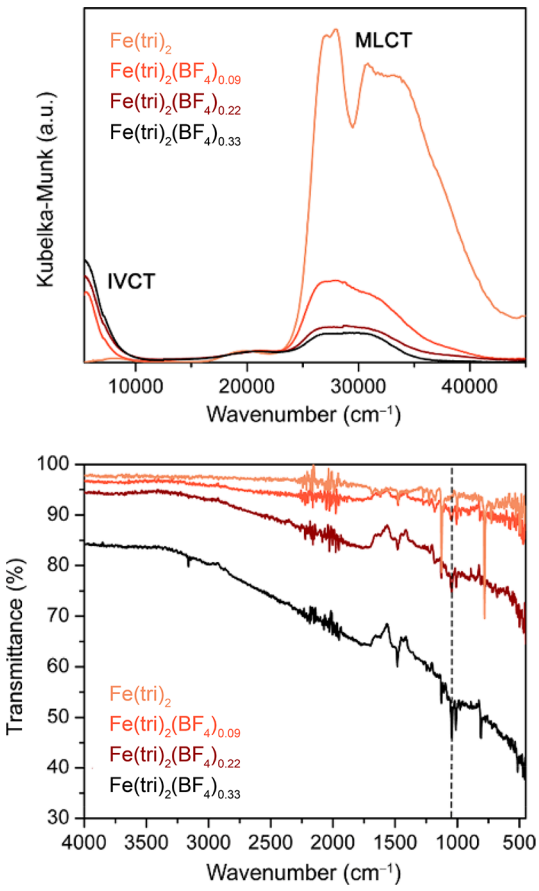

Figure 5. Diffuse reflectance UV–vis–NIR (top) and infrared spectra (bottom) of $Fe(tri)_2$ and $Fe(tri)_2(BF_4)_x$. The diffuse reflectance spectra were normalized to the intensity of the weak d–d transition band. The infrared peak corresponding to a stretching mode of BF_4^- is shown with a dashed line.

DOI: 10.1021/jacs.8b03696
J. Am. Chem. Soc. 2018, 140, 8526–8534

transition intensity of $Fe(tri)_2$ for ease of comparison, as this spectral feature remains similar across the four compounds, in contrast to the intensity changes in the other bands.

Although $Fe(tri)_2$ exhibits no significant absorption in the near-IR region, substantial broad absorption bands are apparent between 5000 and 10 000 cm^{-1} and increase in relative intensity with oxidation in $Fe(tri)_2(BF_4)_x$. These features can be attributed to an intervalence charge transfer (IVCT) transition between iron(II/III) centers, but due to the detection limit of the UV−vis−NIR instrument, the diagnostic low-energy edge of the IVCT absorption could not be observed.[23] We speculate that the IVCT bands of $Fe(tri)_2(BF_4)_x$ extend out to the mid-IR region, as suggested in Figure 5.

The UV−vis−NIR spectrum of $Fe(tri)_2$ also exhibits broad, intense absorption bands at higher ν_{max} values of 27 200 and 31 000 cm^{-1}, which we assign to metal-to-ligand charge transfer (MLCT) transitions.[18a] With increasing oxidation, the MLCT bands substantially decrease in intensity relative to the d-d transitions. Whereas the increasing relative intensity of IVCT transition is consistent with an increasing charge carrier density with oxidation, a decreasing relative intensity of MLCT transition results from a decreasing concentration of Fe^{II} centers that participate in the π back-bonding.

Infrared Spectroscopy. The IR spectra of $Fe(tri)_2$ and $Fe(tri)_2(BF_4)_x$ collected under a N_2 atmosphere also exhibit remarkably different features (Figure 5, bottom). The IR spectrum of $Fe(tri)_2$ displays a flat baseline with sharp features corresponding to discrete vibrational modes arising primarily from the triazolate ligand. In contrast, the IR spectrum of $Fe(tri)_2(BF_4)_{0.09}$ features a broad absorption band in the mid-IR region that becomes stronger with increasing oxidation to x = 0.22 and 0.33. This absorption most likely originates from low-lying electronic excitations extending into the mid-IR region of the spectrum. A strong absorption of this type that increases with decreasing photon energy may suggest an optical band gap approaching zero. However, because band dispersion in the $Fe(tri)_2$ system is expected to be low, the origin of the feature is perhaps better described as a nearly continuous distribution of localized midgap states.[13a,14,24] Indeed, similar features have been observed in the IR spectra of polaronic materials, such as charge transfer salts[25] and mixed-valence, pyrazine-bridged $Ru^{II/III}$ and $Os^{II/III}$ porphyrinate coordination solids.[13a] While these broad band absorptions may mask the original vibrational modes present for $Fe(tri)_2$, a discernible new feature is observed at 1044 cm^{-1}, corresponding to a stretching mode of BF_4^-.[26] As expected, the relative intensity of this peak increases with increasing degree of oxidation and increasing BF_4^- content of a material.

Electronic Conductivity of $Fe(tri)_2$. By using ac impedance spectroscopy, two-contact electronic conductivity was measured on a pressed pellet of $Fe(tri)_2$ in a screw cell with polished copper electrode contacts (Figure S15). The resulting Nyquist impedance plot was fit with a model circuit (Figure S16) to estimate the dc conductivity. In contrast to the previously reported electronic conductivity of 7.7×10^{-5} S/cm for $Fe(tri)_2$, we obtained a much lower value of less than 7×10^{-9} S/cm. Estimation of the dc conductivity by an $I-V$ sweep (±32.7 V/cm) resulted in an ohmic response and a similarly low value of 1×10^{-10} S/cm (Figure S17). This low conductivity is more consistent with that expected for a valence-pure material containing octahedral iron(II) ions with a low-spin $t_{2g}^6e_g^0$ electron configuration, ions that are separated by large distances (Fe1···Fe1 = 5.8869(4) Å). We suspect that the reported conductivity of 7.7×10^{-5} S/cm was measured not on pure $Fe(tri)_2$ but rather on a partially oxidized sample, as the previous study reported $Fe(tri)_2$ to be air stable and therefore did not follow the rigorous air-free procedures employed herein. A recent report suggesting trace Fe^{III} impurities in $Fe(tri)_2$ also supports this conclusion.[14] Additionally, the measured conductivities for samples of $Fe(tri)_2$ oxidized with small quantities (0.025 and 0.05 equiv) of thianthrenium tetrafluoroborate display a significant increase (see Table S5, Figures 6 inset, and S18). Indeed, even oxidizing just 2.5% of the iron(II) centers to iron(III) is sufficient to explain the previously reported conductivity values.

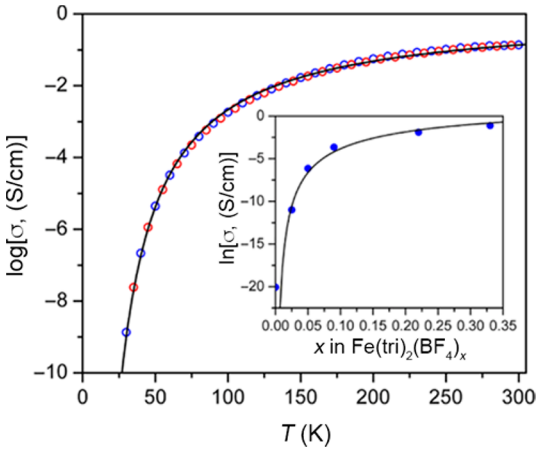

Figure 6. Variable-temperature conductivity data for $Fe(tri)_2(BF_4)_{0.33}$. Blue and red circles represent measurements taken during cooling and warming, respectively. An Arrhenius fit to the data, as described in the SI, is shown by the black curve. (Inset) Plot of room-temperature conductivities versus x in $Fe(tri)_2(BF_4)_x$ (blue circles) and a fit for the doping dependence of conductivity for polaronic Mott insulators (black line). The fit parameters are discussed in the SI.

Two-contact, dc electronic conductivities were also measured on pressed pellets of $Fe(tri)_2(BF_4)_x$. Room temperature conductivities of 0.03(2), 0.2(1), and 0.3(1) S/cm were measured for x = 0.09, 0.22, and 0.33, respectively, and were found to be ohmic within ±8.9 V/cm of an open circuit (Table S5, Figure S18). This increase in conductivity with oxidation level is also consistent with our Mössbauer and UV−vis−NIR spectroscopy data. In particular, the increasing intensities of the valence-averaged doublet in the 290 K Mössbauer spectra and the IVCT bands suggest an increasing carrier concentration with oxidation that engenders a bulk electronic conductivity, possibly accompanied by an increase in carrier mobility.

As shown in the inset of Figure 6 and described in the SI, the room-temperature conductivity values of $Fe(tri)_2(BF_4)_x$ (x = 0.025−0.33) were fit to a model describing the doping dependence of conductivity for Mott insulators with polaronic hopping transport.[10,27] This model derives from Mott's formula for the temperature dependence of the conductivity for variable-range hopping transport (eq 1, d is the dimensionality):

$$\sigma(T) = \sigma_0 e^{-\left(\frac{T_0}{T}\right)^{1/1+d}} \quad (1)$$

DOI: 10.1021/jacs.8b03696
J. Am. Chem. Soc. 2018, 140, 8526−8534

Both the σ_0 and T_0 parameters are dependent on the electron density of states at the Fermi level, $N(E_F)$, according to the following proportionalities:

$$\sigma_0 \propto N(E_F) \tag{2}$$

and

$$T_0 \propto \frac{\alpha^3}{N(E_F)} \tag{3}$$

where α^{-1} is the localization length. If oxidation leads to stoichiometric creation of midgap states, then $N(E_F)$ should be proportional to x and therefore,

$$\ln(\sigma) \propto x^{-(\frac{1}{1+d})} \tag{4}$$

The satisfactory fit of the doping dependence of the conductivity is consistent with a polaronic hopping-based transport model and an increase in carrier concentration upon oxidation of the Fe^{II} centers. To the best of our knowledge, the observed conductivity of 0.3(1) S/cm for $Fe(tri)_2(BF_4)_{0.33}$ is among the highest for three-dimensionally conducting metal−organic frameworks; the iron(III) semiquinoid−quinoid framework is reported to display a conductivity of 0.16(1) S/cm.[9g] In addition, it is worth highlighting that a near 10^8 enhancement in conductivity has been achieved simply through the stoichiometric oxidation of a closed-shell type, insulating metal−organic framework.

Variable-temperature conductivity measurements were performed on $Fe(tri)_2(BF_4)_{0.33}$ over the temperature range of 30−300 K, as shown in Figure 6, and the data exhibit a trend that is consistent with that observed in the variable-temperature Mössbauer spectra. For example, the conductivity is highest at the highest temperature measured, 300 K, the same temperature at which the valence-delocalized doublet observed in the Mössbauer spectra displays its maximum percent area. Upon decreasing the temperature, the conductivity decreases gradually and then rapidly below 90 K. Similarly, the Mössbauer spectrum of $Fe(tri)_2(BF_4)_{0.33}$ obtained at 100 K exhibits a decrease in the intensity of the valence-delocalized $Fe^{II/III}$ doublet concomitant with the emergence of new Fe^{II} and Fe^{III} doublets, indicating a localization of the charges responsible for the observed conductivity. Thus, the decreased conductivity at low temperature likely results from low hopping frequencies of localized charge carriers. The conductivity data suggest that complete localization of charge carriers occurs near or below 30 K, consistent with the disappearance of the valence-delocalized doublet in the Mössbauer spectrum for this material at 5 K.

The variable-temperature conductivity data for $Fe(tri)_2(BF_4)_{0.33}$ were fit assuming an Arrhenius temperature dependence to determine the activation energy for charge hopping, as is shown in Figures 6 and S19. However, fitting the data with a single straight line revealed that the $\ln(\sigma)$ vs $1/T$ plot is not perfectly linear, indicating that the activation energy changes with temperature. It was possible instead to fit the high and low temperature data independently to extract activation energy values of 57.1(4) and 52.3(1) meV, respectively, with a crossover between these two regimes occurring at ∼90 K. These activation energies are relatively small compared to other conductive MOFs (which display values typically on the order of 0.1−1 eV),[7g] likely due to factors such as the strong electronic coupling between low-spin iron centers mediated by the diffuse empty π^* orbitals of the triazolate ligand and the highly isotropic crystal structure. The existence of two temperature regimes with distinct activation energies for $Fe(tri)_2(BF_4)_{0.33}$ likely originates from the valence localization behavior characterized at low temperature by Mössbauer spectroscopy (vide supra and Table S4). The observed contraction of the unit cell with decreasing temperature (see Table S3), and the corresponding decrease in iron−iron distances, may also contribute to the observed decrease in activation energy at ∼90 K.

CONCLUSIONS

The foregoing results demonstrate that the $Fe(tri)_2$ framework, although previously reported[8c] to be air-stable and moderately conductive, is in fact extremely sensitive to oxidation and in pure form exhibits very low conductivity that is consistent with the insulating behavior expected for low-spin octahedral iron(II) ions bridged by 1,2,3-triazolate linkers. This work thus serves to emphasize that special caution is imperative when handling and studying the conductivity of redox-active metal−organic frameworks, because even small valence impurities can result in a drastic enhancement of conductivity. We have also shown that the conductive frameworks $Fe(tri)_2(BF_4)_x$ (x = 0.09, 0.22, 0.33) can be readily obtained via stoichiometric chemical oxidation of $Fe(tri)_2$, and that these materials exhibit enhancements in conductivity of up to 8 orders of magnitude over that of the parent framework. Further, $Fe(tri)_2(BF_4)_{0.33}$ exhibits an electronic conductivity of 0.3(1) S/cm, which is one of the highest values reported to date for a three-dimensional metal−organic framework. The electronic conductivities notably derive from a high degree of charge delocalization between octahedral low-spin iron(II) and iron(III) centers, as revealed by Mössbauer spectroscopy. Ongoing studies will seek to examine other metal-triazolate frameworks, as well as how linker donor atoms may be varied to further enhance the conductivity of oxidized variants of $Fe(tri)_2$ through the use of substituted 1,2,3-triazolates.

ASSOCIATED CONTENT

Supporting Information

The Supporting Information is available free of charge on the ACS Publications website at DOI: 10.1021/jacs.8b03696.

Additional experimental procedures, powder X-ray diffraction data, additional Mössbauer spectra and spectral fit parameters, TGA, N_2 adsorption data, variable-temperature conductivity data, and magnetic susceptibility data (PDF)

Crystallographic data for $Fe(tri)_2$ at 300 K (CIF)

Crystallographic data for $Fe(tri)_2(BF_4)_{0.33}$ at 300 K (CIF)

Crystallographic data for $Fe(tri)_2(BF_4)_{0.33}$ at 100 K (CIF)

AUTHOR INFORMATION

Corresponding Author

*jrlong@berkeley.edu

ORCID

Jesse G. Park: 0000-0003-3947-9170

Khetpakorn Chakarawet: 0000-0001-5905-3578

Gary J. Long: 0000-0002-6573-5927

Jeffrey R. Long: 0000-0002-5324-1321

DOI: 10.1021/jacs.8b03696
J. Am. Chem. Soc. 2018, 140, 8526−8534

Notes

The authors declare no competing financial interest.

■ ACKNOWLEDGMENTS

This research was supported by NSF award number DMR-1611525, with the exception of the measurement and analysis of the magnetic data, which were supported by the Nanoporous Materials Genome Center of the U.S. Department of Energy, Office of Basic Energy Sciences, Division of Chemical Sciences, Geosciences and Biosciences under Award No. DE-FG02-17ER16362. Powder X-ray diffraction data were collected at Beamline 17-BM at the Advanced Photon Source, a U.S. Department of Energy Office of Science User Facility, operated by Argonne National Laboratory. Use of the Advanced Photon Source at Argonne National Laboratory was supported by the U.S. Department of Energy, Office of Science, Office of Basic Energy Sciences, under Contract No. De-AC02-06CH11357. We thank the National Science Foundation Graduate Research Fellowship Program for providing support for J.G.P, J.O., and L.E.D., Rodolfo Torres-Gavosto, Michael Ziebel, and Dr. Hiroyasu Furukawa for helpful discussions and experimental assistance, and Dr. Katie R. Meihaus for editorial assistance.

■ REFERENCES

(1) Yaghi, O. M.; O'Keeffe, M.; Ockwig, N. W.; Chae, H. K.; Eddaoudi, M.; Kim, J. *Nature* **2003**, *423*, 705.

(2) Burtch, N. C.; Jasuja, H.; Walton, K. S. *Chem. Rev.* **2014**, *114*, 10575.

(3) For selected reviews, see: (a) Li, J.-R.; Kuppler, J. J.; Zhou, H.-C. *Chem. Soc. Rev.* **2009**, *38*, 1477. (b) Sculley, J.; Yuan, D.; Zhou, H.-C. *Energy Environ. Sci.* **2011**, *4*, 2721. (c) Sumida, K.; Rogow, D. L.; Mason, J. A.; McDonald, T. M.; Bloch, E. D.; Herm, Z. R.; Bae, T.-H.; Long, J. R. *Chem. Rev.* **2012**, *112*, 724. (d) Furukawa, H.; Cordova, K. E.; O'Keeffe, M.; Yaghi, O. M. *Science* **2013**, *341*, 974. (e) Wu, M.-X.; Yang, Y.-W. *Adv. Mater.* **2017**, *29*, 1606134.

(4) (a) Morozan, A.; Jaouen, F. *Energy Environ. Sci.* **2012**, *5*, 9269. (b) Zhang, Z.; Awaga, K. *MRS Bull.* **2016**, *41*, 883. (c) Liao, P.-Q.; Shen, J.-Q.; Zhang, J.-P. *Coord. Chem. Rev.* **2017**, DOI: 10.1016/j.ccr.2017.09.001.

(5) Cox, P. A. *The Electronic Structure and Chemistry of Solids*; Oxford University Press: New York, 2005.

(6) Hendon, C. H.; Tiana, D.; Walsh, A. *Phys. Chem. Chem. Phys.* **2012**, *14*, 13120.

(7) (a) Kobayashi, Y.; Jacobs, B.; Allendorf, M. D.; Long, J. R. *Chem. Mater.* **2010**, *22*, 4120. (b) Narayan, T. C.; Miyakai, T.; Seki, S.; Dincă, M. *J. Am. Chem. Soc.* **2012**, *134*, 12932. (c) Sun, L.; Miyakai, T.; Seki, S.; Dincă, M. *J. Am. Chem. Soc.* **2013**, *135*, 8185. (d) Talin, A. A.; Centrone, A.; Ford, A. C.; Foster, M. E.; Stavila, V.; Haney, P.; Kinney, R. A.; Szalai, V.; El Gabaley, F.; Yoon, H. P.; Léonard, F.; Allendorf, M. D. *Science* **2014**, *343*, 66. (e) Sun, L.; Hendon, C. H.; Minier, M. A.; Walsh, A.; Dincă, M. *J. Am. Chem. Soc.* **2015**, *137*, 6164. (f) Park, S. S.; Hontz, E. R.; Sun, L.; Hendon, C. H.; Walsh, A.; Van Voorhis, T.; Dincă, M. *J. Am. Chem. Soc.* **2015**, *137*, 1774. (g) Sun, L.; Campbell, M. G.; Dincă, M. *Angew. Chem., Int. Ed.* **2016**, *55*, 3566.

(8) For metal mixed-valency, see: (a) Takaishi, S.; Hosoda, M.; Kajiwara, T.; Miyasaka, H.; Yamashita, M.; Nakanishi, Y.; Kitagawa, Y.; Yamaguchi, K.; Kobayashi, A.; Kitagawa, H. *Inorg. Chem.* **2009**, *48*, 9048. (b) D'Alessandro, D. M.; Kanga, J. R. R.; Caddy, J. S. *Aust. J. Chem.* **2011**, *64*, 718. (c) Gándara, F.; Uribe-Romo, F. J.; Britt, D. K.; Furukawa, H.; Lei, L.; Cheng, R.; Duan, X.; O'Keeffe, M.; Yaghi, O. M. *Chem. - Eur. J.* **2012**, *18*, 10595. (d) D'Alessandro, D. M. *Chem. Commun.* **2016**, *52*, 8957. (e) Murase, R.; Leong, C. F.; D'Alessandro, D. M. *Inorg. Chem.* **2017**, *56*, 14373. (f) Xie, L. S.; Sun, L.; Wan, R.; Park, S. S.; DeGayner, J. A.; Hendon, C. H.; Dincă, M. Tunable Mixed-Valence Doping towards Record Electrical Conductivity in a Three-Dimensional Metal-Organic Framework. *J. Am. Chem. Soc.* [Online early access]. DOI: 10.1021/jacs.8b03604. Published Online: May 28, **2018**. (g) Aubrey, M. L.; Wiers, B. M.; Andrews, S. C.; Sakurai, T.; Reyes-Lillo, S. E.; Hamed, S. M.; Yu, C.-J. Y.; Darago, L. E.; Mason, J. A.; Baeg, J.-O.; Grandjean, F.; Long, G. J.; Seki, S.; Neaton, J. B.; Yang, P.; Long, J. R. Tunable Mixed-Valence Doping towards Record Electrical Conductivity in a Three-Dimensional Metal-Organic Framework. *Nat. Mater.* [Online early access]. DOI: 10.1038/s41563-018-0098-1. Published Online: June 4, **2018**.

(9) For ligand mixed-valency, see: (a) Kato, R.; Kobayashi, H.; Kobayashi, A. *J. Am. Chem. Soc.* **1989**, *111*, 5224. (b) Heintz, R. A.; Zhao, H.; Ouyang, X.; Grandinetti, G.; Cowen, J.; Dunbar, K. R. *Inorg. Chem.* **1999**, *38*, 144. (c) Neufeld, A. K.; Madsen, I.; Bond, A. M.; Hogan, C. F. *Chem. Mater.* **2003**, *15*, 3573. (d) Zhang, Z.; Zhao, H.; Kojima, H.; Mori, T.; Dunbar, K. R. *Chem. - Eur. J.* **2013**, *19*, 3348. (e) Kambe, T.; Sakamoto, R.; Hoshiko, K.; Takada, K.; Miyachi, M.; Ryu, J.-H.; Sasaki, S.; Kim, J.; Nakazato, K.; Takata, M.; Nishihara, H. *J. Am. Chem. Soc.* **2013**, *135*, 2462. (f) Kambe, T.; Sakamoto, R.; Kusamoto, T.; Pal, T.; Fukui, N.; Hoshiko, K.; Shimojima, T.; Wang, Z.; Hirahara, T.; Ishizaka, K.; Hasegawa, S.; Liu, F.; Nishihara, H. *J. Am. Chem. Soc.* **2014**, *136* (41), 14357. (g) Darago, L. E.; Aubrey, M. L.; Yu, C. J.; Gonzalez, M. I.; Long, J. R. *J. Am. Chem. Soc.* **2015**, *137*, 15703. (h) Jeon, I.-R.; Negru, B.; Van Duyne, R. P.; Harris, T. D. *J. Am. Chem. Soc.* **2015**, *137*, 15699. (i) DeGayner, J. A.; Jeon, I.-R.; Sun, L.; Dincă, M.; Harris, T. D. *J. Am. Chem. Soc.* **2017**, *139*, 4175. (j) Ziebel, M. E.; Darago, L. E.; Long, J. R. *J. Am. Chem. Soc.* **2018**, *140*, 3040.

(10) (a) Roth, S.; Carroll, D. *One-Dimensional Metals: Conjugated Polymers, Organic Crystals, Carbon Nanotubes and Graphene*; Wiley-VCH: Singapore, 2015. (b) Launay, J.-P.; Verdaguer, M. *Electrons in Molecules: From Basic Principles to Molecular Electronics*; Oxford University Press: Oxford, 2013.

(11) Epstein, A. J.; Rommelmann, H.; Abkowitz, M.; Gibson, H. W. *Mol. Cryst. Liq. Cryst.* **1981**, *77*, 81.

(12) (a) Litterst, F. J.; Amthauer, G. *Phys. Chem. Miner.* **1984**, *10*, 250. (b) Prassides, K. *Mixed Valency Systems: Applications in Chemistry, Physics and Biology*; Springer: Netherlands, 1991. (c) Grandjean, F.; Samain, L.; Long, G. J. *Dalton Trans.* **2016**, *45*, 18018.

(13) (a) Collman, J. P.; McDevitt, J. T.; Leidner, C. R.; Yee, G. T.; Torrance, J. B.; Little, W. A. *J. Am. Chem. Soc.* **1987**, *109*, 4606. (b) Ding, X.-Q.; Bominaar, E. L.; Bill, E.; Winkler, H.; Trautwein, A. X.; Drueke, S.; Chaudhuri, P.; Wieghardt, K. *J. Chem. Phys.* **1990**, *92*, 178. (c) Le Narvor, N.; Toupet, L.; Lapinte, C. *J. Am. Chem. Soc.* **1995**, *117*, 7129. (d) Behera, J. N.; D'Alessandro, D. M.; Soheilnia, N.; Long, J. R. *Chem. Mater.* **2009**, *21*, 1922. (e) Gaudette, A. I.; Jeon, I.-R.; Anderson, J. S.; Grandjean, F.; Long, G. J.; Harris, T. D. *J. Am. Chem. Soc.* **2015**, *137*, 12617. (f) Ma, X.; Lin, C.-S.; Zhu, X.-Q.; Hu, S.-M.; Sheng, T.-L.; Wu, X.-T. *Angew. Chem., Int. Ed.* **2017**, *56*, 1605.

(14) Sun, L.; Hendon, C. H.; Park, S. S.; Tulchinsky, Y.; Wan, R.; Wang, F.; Walsh, A.; O'Keeffe, M.; Dincă, M. *Chem. Sci.* **2017**, *8*, 4450.

(15) Boduszek, B.; Shine, H. J. *J. Org. Chem.* **1988**, *53*, 5142.

(16) Zhou, X.-H.; Peng, Y.-H.; Du, X.-D.; Zuo, J.-L.; You, X.-Z. *CrystEngComm* **2009**, *11*, 1964.

(17) (a) Gütlich, P.; Garcia, Y.; Goodwin, H. A. *Chem. Soc. Rev.* **2000**, *29*, 419. (b) Nihei, M.; Shiga, T.; Maeda, Y.; Oshio, H. *Coord. Chem. Rev.* **2007**, *251*, 2606.

(18) (a) Vos, G.; Le Febre, R. A.; De Graaff, R. A. G.; Haasnoot, J. G.; Reedijk, J. *J. Am. Chem. Soc.* **1983**, *105*, 1682. (b) Biswas, S.; Tonigold, M.; Kelm, H.; Krüger, H.-J.; Volkmer, D. *Dalton Trans.* **2010**, *39*, 9851.

(19) (a) Kahn, O.; Martinez, C. J. *Science* **1998**, *279* (5347), 44. (b) Grosjean, A.; Daro, N.; Kauffmann, B.; Kaiba, A.; Létard, J.-F.; Guionneau, P. *Chem. Commun.* **2011**, *47*, 12382.

(20) Reed, D. A.; Xiao, D. J.; Gonzalez, M. I.; Darago, L. E.; Herm, Z. R.; Grandjean, F.; Long, J. R. *J. Am. Chem. Soc.* **2016**, *138*, 5594.

DOI: 10.1021/jacs.8b03696
J. Am. Chem. Soc. 2018, 140, 8526−8534

(21) (a) Aurbach, D.; Levi, M. D.; Levi, E.; Teller, H.; Markovsky, B.; Salitra, G.; Heider, U.; Heider, L. *J. Electrochem. Soc.* **1998**, *145*, 3024. (b) Levi, M. D.; Salitra, G.; Markovsky, B.; Teller, H.; Aurbach, D.; Heider, U.; Heider, L. *J. Electrochem. Soc.* **1999**, *146*, 1279. (c) Fey, G. T.-K.; Yo, W.-H.; Chang, Y.-C. *J. Power Sources* **2002**, *105*, 82.
(22) Ingalls, R. *Phys. Rev.* **1964**, *133*, A787.
(23) (a) Demadis, K. D.; Hartshorn, C. M.; Meyer, T. *Chem. Rev.* **2001**, *101*, 2655. (b) Brunschwig, B. S.; Creutz, C.; Sutin, N. *Chem. Soc. Rev.* **2002**, *31*, 168. (c) D'Alessandro, D. M.; Keene, F. R. *Chem. Soc. Rev.* **2006**, *35*, 424.
(24) (a) Wooten, F. *Optical Properties of Solids*; Academic Press: New York, 1972. (b) Torrance, J. B. *Chemistry and Physics of One-Dimensional Metals*; Keller, H. J., Ed.; Plenum Press: New York, 1977.
(25) Tanner, D. B.; Jacobsen, C. S.; Garito, A. F.; Heeger, A. J. *Phys. Rev. B* **1976**, *13*, 3381.
(26) (a) Brown, D. H.; Nuttall, R. H.; McAvoy, J.; Sharp, D. W. A. *J. Chem. Soc. A* **1966**, 892. (b) Reedijk, J. *Inorg. Chim. Acta* **1969**, *3*, 517. (c) Holbrey, J. D.; Seddon, K. R. *J. Chem. Soc., Dalton Trans.* **1999**, 2133.
(27) (a) Roth, S.; Bleier, H.; Pukacki, W. *Faraday Discuss. Chem. Soc.* **1989**, *88*, 223. (b) Roth, S. *Hopping Transport in Solids*; Pollak, M., Ed.; Elsevier: Amsterdam, 1991, Vol. 3, p 517.

DOI: 10.1021/jacs.8b03696
J. Am. Chem. Soc. 2018, 140, 8526−8534